Sustainable Chemistry and Pharmacy 33 (2023) 101045

Contents lists available at ScienceDirect

Sustainable Chemistry and Pharmacy

journal homepage: www.elsevier.com/locate/scp

Experimental data-driven and phenomenological modeling approaches targeting the enhancement of $CaTiO_3$ photocatalytic efficiency

Bíborka Boga [a, b], Vasile-Mircea Cristea [b, *], István Székely [c, d, e], Felix Lorenz [a], Tamás Gyulavári [f], Lucian Cristian Pop [b], Lucian Baia [c, d, e], Zsolt Pap [d, e, f], Norbert Steinfeldt [a], Jennifer Strunk [a]

[a] Leibniz Institute for Catalysis (LIKAT), Albert-Einstein-Str. 29a, Rostock, DE-18059, Germany
[b] Faculty of Chemistry and Chemical Engineering, Babeș-Bolyai University, Arany János Str. 11, Cluj-Napoca, RO-400028, Romania
[c] Faculty of Physics, Babeș-Bolyai University, Mihail Kogălniceanu Str. 1, Cluj-Napoca, RO-400084, Romania
[d] Institute for Interdisciplinary Research on Bio-Nano-Sciences, Babeș-Bolyai University, Treboniu Laurian Str. 42, Cluj-Napoca, RO-400271, Romania
[e] Institute for Research-Development-Innovation in Applied Natural Sciences, Babeș-Bolyai University, Fântânele Str. 30, Cluj-Napoca, RO-400294, Romania
[f] Department of Applied and Environmental Chemistry, University of Szeged, Rerrich Sqr. 1, Szeged, HU-6720, Hungary

ARTICLE INFO

Handling Editor: Klaus Kümmerer

Keywords:
$CaTiO_3$
Photocatalytic activity
Polynomial regression
Artificial neural network models
Kinetic modeling
Optimization

ABSTRACT

Optimization based on mathematical models has received growing attention in materials science. The first part of the work aims to optimize the photocatalytic activity of $CaTiO_3$ for rhodamine B (RhB) degradation under UV-A irradiation, based on two developed mathematical models. Thirty hydrothermal syntheses of $CaTiO_3$ were carried out according to the Box-Behnken design, considering synthesis temperature (X_1), duration (X_2), and concentration of shaping agent (X_3) as input variables for two different Ca^{2+} sources: $Ca(NO_3)_2$ and $CaCl_2$ (X_4). The conversion of the studied pollutant after 4 h was situated in the range of 20–80%. Second-order regression and feedforward backpropagation artificial neural network models were developed, considering the synthesis conditions (X_1, X_2, X_3, X_4) as input and the conversion as output variables. The proposed model-based methodology for the optimization of $CaTiO_3$ photocatalytic efficiency finally directed to the experimentally attained value of 96% for 200 °C ($X_{1,\ opt}$), 23.17 h ($X_{2,\ opt}$), 0.67 M ($X_{3,\ opt}$), $CaCl_2$ ($X_{4,\ opt}$). Furthermore, in the second part of the study, the morphological, structural, textural, and optical properties of selected $CaTiO_3$ samples were investigated *via* scanning electron microscopy, X-ray diffractometry, N_2 sorption, and diffuse reflectance spectroscopy. Finally, the kinetic parameters for adsorption (k_{ads}: 0.10–0.67 $m \cdot h^{-1}$), desorption (k_{des}: 79–150 $mmol \cdot m^{-2} \cdot h^{-1}$), degradation ($k_{degr}$: 0.001–0.010 $mmol \cdot m^{-2(1-\alpha)} \cdot W^{-\alpha} \cdot h^{-1}$), and intensity exponent (α: 0.54–0.55) were fitted using an optimization procedure, considering the experimentally determined and model-predicted apparent reaction rate constants. The obtained kinetic parameters were correlated with the specific surface area of the catalysts and the conversion of RhB.

* Corresponding author.
E-mail address: mircea.cristea@ubbcluj.ro (V.-M. Cristea).

https://doi.org/10.1016/j.scp.2023.101045
Received 24 February 2022; Received in revised form 24 February 2023; Accepted 26 February 2023
Available online 23 March 2023

Abbreviations:

0A	sampling moment immediately before switching on the lamps
ANOVA	analysis of variance
BBD	Box-Behnken design
CE1	central point experiment within R1 (X_1:190 °C, X_2: 24 h, X_3: 1.005 M, X_4: $Ca(NO_3)_2$)
CE2	central point experiment within R2 (X_1:190 °C, X_2: 24 h, X_3: 1.005 M, X_4: $CaCl_2$)
DF	degree of freedom
DoE	design of experiment methodology
DRS	diffuse reflectance spectroscopy
FB-ANNs	feedforward backpropagation artificial neural network models
k_{ads}	rate constants for adsorption [$m \cdot h^{-1}$]
k_{degr}	absolute kinetic rate constant [$mmol \cdot m^{-2(1-\alpha)} \cdot W^{-\alpha} \cdot h^{-1}$]
k_{des}	rate constants for desorption [$mmol \cdot m^{-2} \cdot h^{-1}$]
k_{obs}	pseudo-first order reaction rate constant [h^{-1}]
MS	mean of squares
MSE	mean of squares for error
MSR	mean of squares for regression
P	product(s)
PSSA	pseudo-steady state assumption
R	reactant(s)
R1	first set of experiments (when $Ca(NO_3)_2$ is used as Ca^{2+} precursor)
R2	second set of experiments (when $CaCl_2$ is used as Ca^{2+} precursor)
R^2	determination coefficient
R^2_{adj}	adjusted determination coefficient
R^2_{pred}	predicted determination coefficient
RhB	rhodamine B
SEM	scanning electron microscopy
SS	sum of squares
SSA	specific surface area
SSE	sum of squares calculated for error
SSR	sum of squares calculated for regression
X	conversion
X_1, X_2, X_3	input variables (i.e., X_1 – synthesis temperature, X_2 – synthesis duration, X_3 – concentration of shaping agent, X_4 – type of Ca^{2+} precursor)
$X_{1,\ opt}$, $X_{2,\ opt}$, $X_{3,\ opt}$, $X_{4,\ opt}$	optimal synthesis parameters
XRD	X-ray diffraction
$\hat{Y}_i$	model-predicted response (calibrated)
Y_i	experimentally determined response

1. Introduction

The development of highly efficient photocatalysts can be considered a promising alternative for solving the environmental concern related to the improper or low treatment effectiveness of wastewaters. Recently, alkaline earth metal titanates (i.e., $CaTiO_3$, $SrTiO_3$, $BaTiO_3$) have attracted considerable interest in the field of photocatalysis (Solís et al., 2021). Due to their promising band structure (Solís et al., 2021) they can be used to degrade dyes (Bai et al., 2018; da Silva et al., 2016; Kappadan et al., 2016), to produce hydrogen (Chen et al., 2018; Wang, R. et al., 2018; Yu et al., 2017), to reduce Cr^{6+} in water (especially with $SrTiO_3$ (Xing et al., 2016)), and to transform CO_2 into valuable products *via* photoreduction (Luo et al., 2018; Soltani et al., 2021).

Numerous papers have already been published concerning the relationship between synthesis method (conditions or input factors) and structure, or between the morphology of photocatalysts and the resulting photocatalytic efficiency (e.g., TiO_2 (Cui et al., 2012; Naik et al., 2020), $CaTiO_3$ (Han et al., 2016; Kimijima et al., 2014)). However, there is a considerable demand to make such predictions even before carrying out the synthesis and without having extended morphological or structural information using only photocatalytic results. Such predictions can be made using different mathematical models (either mechanistic or empirical models), thus saving raw materials, time, financial resources and research effort (Edwards and Hamson, 2020). Although the experimental data-driven modeling (also called empirical) approach is based on the observed responses (and not directly based on the description of underlying phenomena or mechanisms) (Perez-Rodriguez and Valero, 2013), its implementation has received considerable interest in the field of materials science mainly due to its capability to embed the complex behavior not yet able to be captured by first principle models. Regardless of the type of the modeling approach, the importance of experimental data is obvious (Mehrizad and Gharbani,

2014). It is worthy to note that data can be obtained either from systematically or non-specifically designed experimentation approaches (Dobre and Marcano, 2007; Mehrizad and Gharbani, 2016; Mosavi et al., 2021; Sematech, 2006).

This work focuses upon the investigation of $CaTiO_3$, a well-known representative of the class of perovskites and alkaline earth metal titanates. It possesses several promising features, such as ferroelectricity (Biegalski et al., 2015), dielectricity (Maddu et al., 2017), chemical stability (Kumar et al., 2020; Lee et al., 2021), and biocompatibility (Zhu et al., 2016). Several synthesis routes have been reported in the literature, such as solid-state (Shimura and Yoshida, 2010; Yang et al., 2014), sol-gel (Huo et al., 2014), co-precipitation (Huang et al., 2016), microwave assisted (de Cássia Pereira et al., 2017), electrospinning (Zhang et al., 2015), hydro- and solvothermal method (Dong et al., 2015; Han et al., 2016; Yang et al., 2010). Among them, hydro- and solvothermal syntheses are probably the most promising routes because they enable the control of crystal growth and morphology, and they can be carried out under relatively mild reaction conditions (Passi and Pal, 2021). Due to its advantageous band structure, $CaTiO_3$ has been reported as a promising candidate not only for water splitting (Jang et al., 2011), but also for the photodegradation of certain pollutants (e.g., methylene blue (Zhao et al., 2013a), methyl orange (Huo et al., 2014). In this study, the photodegradation of a well-known xanthene-type dye, specifically of rhodamine B (RhB) was investigated *via* the support of different modeling approaches. The results of the study address to a wide range of applications, since there are a lot of xanthene-type pharmaceuticals (e.g., vadimezan, lucanthone, mepixanox) whose degradation pathways are similar to that of RhB, and whose removal from wastewater is imperative. Furthermore, the number of studies where empirical and phenomenological modeling approaches were used to interpret photocatalytic efficiency is relatively reduced, and the present study may be considered to bring contributions to this status quo.

Although black box (data-driven) models are very promising, they do not provide a phenomenological overview concerning photodegradation processes in terms of kinetics and mass transfer. From the phenomenological point of view, the photodegradation of a certain pollutant can be described by the following elementary steps: (1) mass transfer of reactants (R) from the liquid phase to the surface of a catalyst; (2) adsorption of R onto the surface of an excited (photoactivated) catalyst; (3) transformation of the adsorbed reactants into products (P); (4) desorption of the P from the surface; (5) mass transfer of the P from the interface region to the liquid phase (Fogler, 2010; Hossain, 2018). Furthermore, some of these elementary steps are determined by the crystallinity, crystal phase and specific surface area of the catalyst, the presence/absence of dopants or by the fluid dynamics (Joo et al., 2012). To sum up, this phenomenological description implies the knowledge of certain constants and coefficients which are characteristic of surface processes.

The first part of this work offers an overview of the relationship between selected hydrothermal synthesis parameters and the photocatalytic efficiency of the final material for RhB degradation *via* different modeling approaches. The second part provides an insight into the phenomenological interpretation of the photocatalytic efficiency.

The proposed integrated approach of the photocatalyst synthesis, development of the data-driven modeling methodology in association with phenomenological interpretations and optimization of the synthesis condition for obtaining the highest photodegradation efficiency may be considered as the main and novel contributions of this work.

2. Material and methods

2.1. Chemicals

The chemicals used for the hydrothermal synthesis of $CaTiO_3$ were as follows: $Ca(NO_3)_2{\cdot}4H_2O$ (Lach-Ner, ≥99%), $CaCl_2$ (Chempur, analytically pure), NaOH (Chempur, analytically pure), $Ti(C_4H_9O)_4$ (Sigma-Aldrich, 97%), C_2H_6O (Merck Millipore, analytically pure). The degradation of RhB dye ($C_{28}H_{31}ClN_2O_3$) (ReAnal, analytically pure) in aqueous solution was studied in this work.

2.2. Synthesis of $CaTiO_3$

First, a stoichiometric amount of Ca^{2+} precursor (X_4) was dissolved in water, which was followed by the dropwise addition of 3.4 mL of tetrabutyl titanate (initial Ca^{2+}: Ti^{4+} molar ratio = 1:1) under continuous stirring. Then, a certain amount of NaOH (0.8 g, 1.2 g or 1.6 g) was added to the reaction mixture, thus adjusting the concentration of NaOH to 0.670, 1.005 or 1.340 M (X_3) in the initial reaction mixture. The hydrothermal crystallizations were carried out under specified conditions (X_1: 180, 190 or 200 °C, X_2: 20, 24 or 28 h) according to the chosen experimental design. This was followed by washing (once with ethanol and three times with water) and drying at 80 °C for 12 h.

2.3. Assessment of photocatalytic efficiency

The photocatalytic efficiency was assessed in a cylindrical slurry photoreactor for RhB degradation (C_0 = 10 μM). The photoreactor was irradiated externally by six symmetrically placed fluorescent UV lamps (6 × 6 W, λ_{max} = 365 nm). During the photocatalytic tests (4 h), a constant suspension temperature (25 °C) was assured by circulating cooling water in the jacket. Continuous air flow (≈50 $L{\cdot}h^{-1}$) and stirring (500 rpm) were assured to facilitate the mass transfer ($C_{suspension}$ = 1 $g{\cdot}L^{-1}$). Samples were taken at predetermined intervals (0, 0A, 30, 60, 120, 180, 240 min), followed by their centrifugation, filtration (0.22 μm TPFE) and analysis *via* an Analytic Jena Specord 250 Plus UV–vis spectrophotometer (Tabatabaei et al., 2011) (considering the absorbance at 552 nm). The photocatalytic activity was assessed *via* the conversion of RhB after 4 h. Each photodegradation test was repeated at least twice.

2.4. Experimental design

The Box-Behnken experimental design (BBD) was specifically applied for two approaches, according to the type of Ca^{2+} precursor, i.e., either $Ca(NO_3)_2$ or $CaCl_2$ (X_4), and for three continuous factors (X_1, X_2, X_3) with three levels (low: −1, center: 0, high: +1). As pre-

sented in Table 1, the synthesis temperature (X_1), the duration (X_2) and the concentration of the shaping agent (X_3) were assigned as continuous factors, and the type of precursor (X_4) as categorical factor.

2.5. Regression analysis

A second-order model was chosen to describe the relationship between the independent variables and the conversion, as depicted in Equation (1). The individual and the interaction effects between the variables were evaluated by employing analysis of variance (ANOVA) using Minitab v18 (Peng et al., 2020).

$$Y = \beta_0 + \sum_{i=1}^{3} \beta_i \cdot X_i + \sum_{i=1}^{3} \beta_{ii} \cdot X_{ii}^2 + \sum_{i=1}^{3} \sum_{j=i+1}^{3} \beta_{ij} \cdot X_i \cdot X_j \quad (1)$$

Although several statistical metrics are involved within ANOVA, the most important of them are described *via* Equations (2)–(5):

$$SSR = \sum_{i=1}^{n} \left(\hat{Y}_i - \bar{Y} \right)^2 \quad (2)$$

$$SSE = \sum_{i=1}^{n} \left(Y_i - \hat{Y}_i \right)^2 \quad (3)$$

$$MS = \frac{SS}{DF} \quad (4)$$

$$F = \frac{MSR}{MSE} \quad (5)$$

Significance of the terms in Equations (2)–(5): DF – degree of freedom, F – F-value, MS – mean of squares (MSE – mean of squares for error, MSR – mean of squares for regression), SS – sum of squares (SSE – sum of squares for error, SSR – sum of squares for regression), $\hat{Y}_i$ – model-predicted response (fitted), Y_i – experimentally determined response, $\bar{Y}$– average value of the experimentally determined responses.

Further statistical parameters were used for the assessment of the implemented models, namely the determination coefficient (R^2, Equation (6)) adjusted R^2 (R^2_{adj}, Equation (7)), predicted R^2 (i.e., R^2_{pred}) (Dillon and Goldstein, 1984; Yin and Fan, 2001):

$$R^2 = 1 - \frac{\sum_{i=1}^{n} \left(Y_i - \hat{Y}_i \right)^2}{\sum_{i=1}^{n} \left(Y_i - \bar{Y} \right)^2} \quad (6)$$

$$R^2_{adj} = 1 - \left[\frac{\left(1 - R^2\right) \cdot (n-1)}{(n-k)} \right] \quad (7)$$

Significance of terms in Equation (7): k – number of independent variables, n – sample size.

The computation of R^2_{pred} involves the systematic removal of each observation from the data set, followed by the prediction of removed observations based on the estimated regression equation (Dillon and Goldstein, 1984; Yin and Fan, 2001).

2.6. Artificial neural network models

Feedforward backpropagation artificial neural network models (FB-ANNs) were implemented in Matlab software environment (Matlab 2015b) to predict the photocatalytic efficiency for given inputs. The experimental data were randomly split into training, validation, and testing data sets (70%, 15%, 15%). The FB-ANN was trained for one hidden layer with a maximum number of three hidden neurons. The selection of activation function (in the hidden layer), training function and the number of hidden neurons was performed considering a combination of systematically and trial-and-error conducted training procedure. The assessment of FB-ANN performance was carried out based on the Pearson correlation coefficients and the relative errors.

Table 1
Experimental range and levels of independent variables.

No.	Continuous factor	Low level (−1)	Center level (0)	High level (+1)
1.	X_1 (°C)	180	190	200
2.	X_2 (h)	20	24	28
3.	X_3 (M)	0.670	1.005	1.340
	Categorical factor	0	1	
4.	X_4	$Ca(NO_3)_2$	$CaCl_2$	

2.7. Assessment of morpho-structural, textural and optical peculiarities

The crystallinity and crystal phase of the samples were determined from the X-ray diffraction (XRD) patterns recorded with a Shimadzu 6000 diffractometer (Shimadzu Corporation, Kyoto, Japan), equipped with a Cu-Kα source (λ = 1.54 Å).

Considering the shape factor (K = 0.9, spherical crystallites), the X-ray wavelength (λ) and certain information provided by the recorded XRD patterns (i.e., θ – peak position, β – full width at half maximum), the average crystallite size (τ) was calculated *via* the Scherrer equation, as depicted in Equation (8) (Monshi et al., 2012):

$$\tau = \frac{K \cdot \lambda}{\beta \cdot \cos\ \theta} \tag{8}$$

The morphological particularities of the samples were revealed based on the micrographs recorded with a FEI Quanta 3D FEG scanning electron microscope (SEM) (accelerating voltage 25 kV). Furthermore, the textural properties of the samples were analyzed *via* nitrogen adsorption considering the BET multipoint method (p/p_0: 0.05–0.3). Nitrogen adsorption data were collected at 77 K on a NOVAtouch (Quantachrome Instruments) surface area and pore size analyzer after samples were pretreated by heating to 200 °C under vacuum for 10 h. The diffuse reflectance spectra (DRS) of the perovskites investigated in the UV–visible (250–800 nm) region were recorded with a JASCO-V650 spectrophotometer equipped with an ILV-724 integration sphere. Considering the UV-vis diffuse reflectance spectra of the samples, the band gap values were determined *via* the Kublelka-Munk function (F(R), as presented in Equation (9)):

$$F(R) = \frac{\left(1 - R_\infty\right)^2}{2 \cdot R_\infty} = \frac{k}{s} \tag{9}$$

The significance of the terms in Equation (9) is the following: k – absorption coefficient [m^{-1}], R_∞ – diffuse reflectance of the layer of infinite thickness [dimensionless], s – scattering coefficient [m^{-1}].

2.8. Kinetic modeling

The first step within the kinetic modeling assumed the determination of pseudo-first order reaction rate constants ($k_{obs,}$ Equation (11)) considering the Langmuir Hinshelwood kinetic model (Equation (10)) (Kedves et al., 2019; Mehrizad and Gharbani, 2017).

$$r = -\frac{dC}{dt} = \frac{k_{cat} \cdot K_a \cdot C}{1 + K_a \cdot C} \tag{10}$$

When $K_a \cdot C \approx 0$ (which is satisfied when the order of C_0 is lower than 10^{-3} M (Deshpande and Madras, 2010), as in our case $C_0 = 10^{-5}$ M), the following approximation can be applied:

$$r = k_{cat} \cdot K_a \cdot C = k_{obs} \cdot C \tag{11}$$

The significance of terms from Equations (10) and (11): C – concentration [mol·L^{-1}], K_a – adsorption equilibrium constant [dimensionless], k_{cat} – reaction rate constant [s^{-1}], r – reaction rate [mol·L^{-1}·s^{-1}].

Furthermore, a validated two-dimensional mathematical model of a slurry photoreactor provided by Palmisano and coworkers (Palmisano et al., 2015) was used to determine the rate constants for substrate adsorption (k_{ads}), desorption (k_{des}), degradation (k_{degr}) and intensity exponent (α) *via* optimization (least-square method). The optimization was performed in Matlab 2015b, which is described in detail in Section 3.3.

According to the pseudo-steady assumption (PSSA), the apparent adsorption constant ($K_{ads,\ apparent}$) is described as a function of light radiation flux intensity (I), exponent parameter (α) and a set of kinetic constants (k_{ads}, k_{des}, k_{degr}):

$$K_{ads,apparent} = \frac{k_{ads}}{k_{des} + k_{degr} \cdot I^\alpha} \tag{12}$$

The implemented model has the following form (Palmisano et al., 2015):

$$k_{obs} = \frac{1}{S} \cdot \frac{A}{V} \int_0^{l_{1,max}(\theta)} \int_{-\theta_0}^{\theta_0} k_{degr} \cdot I^\alpha \frac{k_{ads}}{k_{des} + k_{degr} \cdot I^\alpha} \cdot \frac{1}{1 + \frac{k_{ads}}{k_{des} + k_{degr} \cdot I^\alpha} \cdot C_{Sub,0}} \cdot \left(r_1 + 1\right) d\theta dl \tag{13}$$

$$l_{1,max}(\theta) = 2 \cdot \sqrt{\left(r_0 + R\right)^2 \cdot \cos^2\theta_1 - r_0^2 - 2 \cdot r_0 \cdot R} \tag{14}$$

The significance of the terms in Equations (13) and (14) is the following (Palmisano et al., 2015): A – surface area of the catalyst (i.e., specific surface area multiplied by mass) [m^2], $C_{sub,0}$ – initial concentration of the substrate [mmol·m^{-3}], I – light radiation flux [W·m^{-2}], l – light path length, light propagation coordinate [m], l_{1max} – the longest possible light pathway [m], r – cylindrical radial coordinate [m], r_1 – distance between the "1" light source and photoreactor wall [m], S – cross sectional area of the reactor [m^2], V – volume of the reaction mixture [m^3], θ – cylindrical radial coordinate [rad]; θ_0 – maximum value of θ ($-\theta_0 \le \theta \le \theta_0$) [rad]. The details regarding the terms presented in Equation (13) can be found in the publication of Palmisano et al. (2015).

3. Results and discussion

3.1. Effect of synthesis conditions on photocatalytic efficiency

To establish a relationship between the synthesis conditions (T – X_1, t – X_2, C – X_3) and the photocatalytic efficiency (expressed *via* conversion X), the first 30 sets of synthesis were carried out according to the BBD and the results are presented in Table 2. They were followed by photocatalytic tests (as described in Section 2.3.).

The impact of synthesis conditions on the photocatalytic efficiency is shown in Table 2. The most efficient photocatalyst (X = 79.4%) within the designed experiments was synthesized using $CaCl_2$ as a Ca^{2+} source (denoted R2) and 0.67 M NaOH (C), which were subjected to hydrothermal treatment for 24 h (t) at 200 °C (T) (i.e., Exp1-R2, Table 2). The least efficient photocatalyst was synthesized using $Ca(NO_3)_2$ as a Ca^{2+} source (denoted R1) and 1.34 M NaOH (C), with treatment at 180 °C (T) for 24 h (t) (i.e., Exp13-R1, Table 2). The latter case showed the degradation of only 20.4% of the pollutant after 4 h under the presented experimental conditions.

Two data-driven models, that is, polynomial regression (3.1.1.) and FB-ANNs (3.1.2.), were implemented to establish correlations between the hydrothermal synthesis conditions of $CaTiO_3$ and their photocatalytic efficiency.

3.1.1. Polynomial model fitting and ANOVA

Considering the categorical input variable (X_4, that is, the type of Ca^{2+} precursor), two separate polynomial models were implemented for describing the influence of continuous factors on conversion (Y_1, $Y_2 = f(X_1, X_2, X_3)$, R1 $Ca(NO_3)_2$, R2 $CaCl_2$). As a first approach, full quadratic second-order models were fitted by involving all the linear (X_1, X_2, X_3), square (X_1^2, X_2^2, X_3^2) and interaction ($X_1 \cdot X_2$, $X_1 \cdot X_3$, $X_2 \cdot X_3$) terms. All predicted coefficients were estimated *via* the least-squares method. The pre-exposed significance (α) level was chosen to be 0.05. Because the p-value associated to certain terms from the full quadratic models were found to be statistically not significant ($p > 0.05$), these models were refitted without those terms, as it was depicted in Equations (15) and (16). These terms were X_1 for R1 and $X_1 \cdot X_2$, $X_1 \cdot X_3$, $X_2 \cdot X_3$ for R2.

$$Y_{R1} = 881.3 - 26.27 \cdot X_2 - 972 \cdot X_3 - 1.58 \cdot 10^{-2} \cdot X_1^2 + 0.15 \cdot X_2^2 + 92.64 \cdot X_3^2 + 8.94 \cdot 10^{-2} \cdot X_1 \cdot X_2 + 3.58 \cdot X_1 \cdot X_3 + 2.60 \cdot X_2 \cdot X_3 \quad (15)$$

$$Y_{R2} = 1243 - 15.55 \cdot X_1 + 32.64 \cdot X_2 - 264.9 \cdot X_3 + 4.22 \cdot 10^{-2} \cdot X_1^2 - 0.69 \cdot X_2^2 + 110.66 \cdot X_3^2 \quad (16)$$

The comparison between the experimentally determined and model-predicted conversion values is presented in Fig. 1.

Furthermore, the analysis of variance (ANOVA) was performed considering the well-known statistical metrics, such as the degrees of freedom (DF), sum of squares (SS), mean of squares (MS), F-value and p-values, as presented in Tables 3 and 4. According to ANOVA results there are two main sources of variation, namely due to regression and due to error. The quantification of this variation can be carried out *via* sum of squares for regression (SSR), sum of squares for error (SSE), mean square for regression (MSR) and mean square for error (MSE). While SSR provided information about the squared difference between the model-predicted and mean value of the outputs (Equation (2)), SSE offered an overview on the squared difference between the model-predicted and experimental values of the output (Equation (3)). As revealed by the results presented in Tables 3 and 4, relatively close values can be observed for SSR and SSE in the case of R1 and R2 (SSR: 2845.59 (R1) *vs* 2995.55 (R2); SSE: 11.53 (R1) *vs* 32.27 (R2)). The former statistical metrics contributed to the computation of F-value (as a ratio between MSR and MSE, Equation (5)).

Although both F- and p-values can be considered for taking the decision regarding to the rejection of the null hypothesis, within this work the significance of the terms was assessed through the p-values. According to the ANOVA results presented in Tables 3 and 4, it can be concluded that while all terms within the regression were statistically significant ($p < 0.05$), the lack-of-fit was statistically insignificant in both cases ($p > 0.05$).

Table 2
Experimental runs of BBD DoE and experimental results for the photocatalytic degradation efficiency (The bold characters designate the highest conversion values).

Run no.	T (°C)	t (h)	C (M)	X (%, R1)	X (%, R2)
1	200	24	0.670	45.8	**79.4**
2	180	24	0.670	**73.5**	**66.9**
3	200	24	1.340	40.7	50.3
4	200	28	1.005	38.4	37.3
5	180	28	1.005	38.3	30.6
6	190	28	0.670	**62.2**	57.1
7	190	28	1.340	40.7	29.6
8	190	20	1.340	28.7	29.2
9	190	24	1.005	35	43.2
10	190	24	1.005	36.9	43.9
11	190	24	1.005	36.4	42.5
12	180	20	1.005	43	33
13	180	24	1.340	20.4	42.8
14	200	20	1.005	28.6	44.6
15	190	20	0.670	**64**	**62.5**

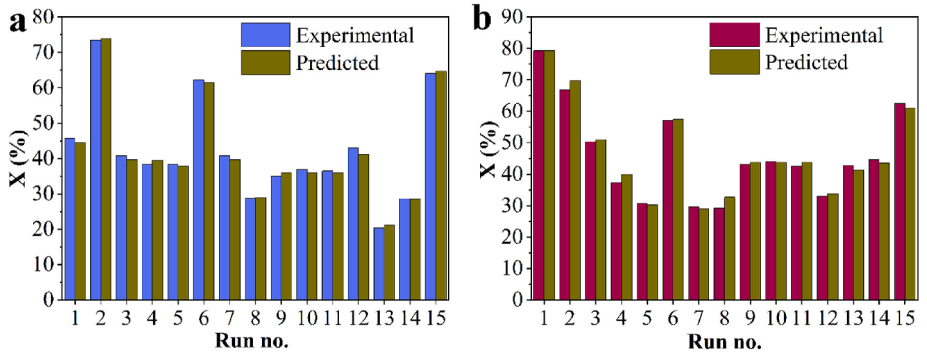

Fig. 1. Comparison between experimentally determined and model-predicted conversion values: a. R1, b. R2.

Table 3
The ANOVA results for R1.

			DF	SS	MS	F-value	P-value
Regression			8	2845.59	355.70	185.12	0.000
	Linear						
		X_2	1	86.25	56.25	44.89	0.001
		X_3	1	979.70	979.70	509.87	0.000
	Square						
		X_1^2	1	327.40	327.40	170.39	0.000
		X_2^2	1	21.02	21.02	10.94	0.016
		X_3^2	1	401.42	401.42	208.91	0.000
	2-Way Interaction						
		$X_1 \cdot X_2$	1	52.38	52.38	27.26	0.002
		$X_1 \cdot X_3$	1	579.02	579.02	301.34	0.000
		$X_2 \cdot X_3$	1	48.63	48.63	25.31	0.002
Error	6			11.53	1.92	–	–
	Lack-of-fit	4		9.65	2.41	4.58	0.30
	Pure error		2	1.87	0.94	–	–
TOTAL			14	2857.12	–	.	.

R^2 = 99.60%, R^2_{adj} = 99.06%, R^2_{pred} = 96.61%.

Table 4
The ANOVA table for R2.

			DF	SS	MS	F-value	P-value
Regression			6	2995.55	499.26	123.78	0.000
	Linear						
		X_1	1	61.82	61.82	15.33	0.004
		X_2	1	435.58	435.58	107.99	0.000
		X_3	1	797.36	979.36	197.69	0.000
	Square						
		X_1^2	1	65.70	65.70	16.29	0.004
		X_2^2	1	449.35	449.35	111.40	0.000
		X_3^2	1	569.41	569.41	141.17	0.000
Error			8	32.27	4.03	–	–
	Lack-of-fit		6	31.29	5.22	10.64	0.088
	Pure error		2	0.98	0.49	–	–
TOTAL			14	3027.82	–	–	–

R^2 = 98.93%, R^2_{adj} = 98.14%, R^2_{pred} = 95.79%.

The remarkably good agreement between the experimental determined and model-predicted conversion values was proven also by high values of determination coefficients (R^2, R^2_{adj}, R^2_{pred}), as presented in Tables 3 and 4

The results presented showed that all three selected synthesis parameters have a significant effect on the photocatalytic performance of $CaTiO_3$.

Considering the second-order regression models developed in this work, optimization of the conversion was carried out *via* the Optimization Toolbox (optimtool) of Matlab 2015b. Both SQP (fmincon solver) and genetic algorithm were used for finding the maximum conversion and the corresponding synthesis conditions (T, t, C), within the predefined ranges of the decision variables (T: 180–200 °C, t: 20–28 h, C: 0.67–1.34 M). The model-based computed maximum conversion values were placed around 80% in both cases (R1: 81.9%, R2: 79.5%). The optimal synthesis conditions were determined to be 180 °C, 20 h and 0.67 M for R1, and 200 °C, 23.67 h and 0.67 M for R2.

The new experiments using the synthesis conditions proposed by optimization showed at this points a conversion of 66% (R1) and of 95.7% (R2). Considering the experimental and model-predicted maximum conversion values, their difference was attributed to the limitations of the chosen experimental design (BBD) that involved a parsimonious number of experiments. The under- and overestimated conversion values were assumed to occur due to the lack of experimental data at the extreme points (180 °C, 20 h, 0.67 M) and in intermediate position (200 °C, 23.7 h, 0.67 M) used for model implementation (as can also be observed in Table 2). However, for R2 (i.e., when $CaCl_2$ was applied as Ca^{2+} source), the model-based investigations led to the identification of the optimized synthesis conditions under which experimentally confirmed maximum photocatalytic efficiency was assessed.

Considering the results emerged from the experimental runs and from the optimization, the following important conclusions can be drawn: (i) the use of $CaCl_2$ as the Ca^{2+} source seems to be more efficient, (ii) the concentration value of NaOH for the maximum conversion is situated at its lowest predefined level (0.67 M).

To assess the simultaneous effects of the synthesis parameters on the photocatalytic efficiency and analyze their pairwise interaction consequences, 3D plots were generated by fixing one of the continuous independent variables at its central value (i.e., T_C = 190 °C, t_C = 24 h, C_C = 1 M).

3.1.1.1. The simultaneous effect of T (X_1) and t (X_2). Analyzing the response surfaces shown in Fig. 2, we observed different patterns according to the different Ca^{2+} sources. First, applying both a high synthesis temperature (200 °C) and a long synthesis duration (28 h) led to a relatively low photocatalytic efficiency (R1). In contrast, in the second case (R2), the highest applied synthesis temperature (200 °C) and an intermediate synthesis duration (23–24 h) were favorable, as it was also validated during experimental testing. To provide an explanation for this behavior, the thermodynamics of the sequence of chemical reactions should be analyzed. According to the literature, the role of calcium source (CaX_2) is related to the formation of $Ca(OH)_2$ in alkaline media ($Ca^{2+} + 2OH^- = Ca(OH)_2$) (Wang et al., 2007). It is known that the solubility of calcium salts is very similar in aqueous solutions under the applied conditions. However, the anions of the calcium source (NO_3^-, Cl^-) and the salts they form ($NaNO_3$, NaCl) can have a specific influence on both the properties of crystallization process (because of different ionic strengths) and on the photocatalytic efficiency (Koutsoukos et al., 2007).

3.1.1.2. The simultaneous effect of T (X_1) and C (X_3). Fig. 3 depicted the response surface of an interesting relationship between the synthesis temperature and the concentration of the shaping agent: higher NaOH concentrations led to a decrease in photocatalytic

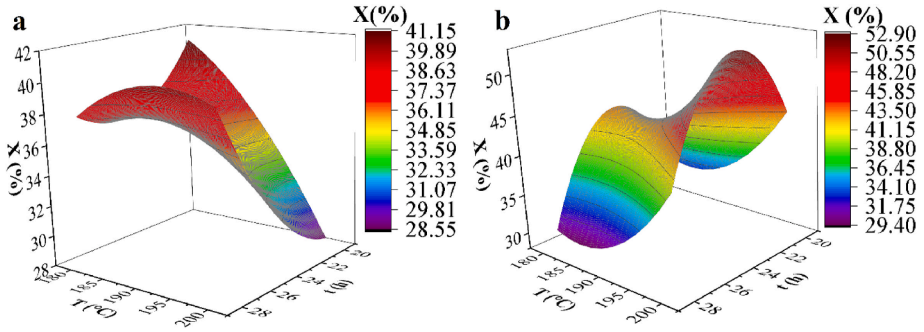

Fig. 2. The simultaneous effect of temperature (X_1, T) and duration (X_2, t) on conversion (a. R1, b. R2, C = 1 M fixed).

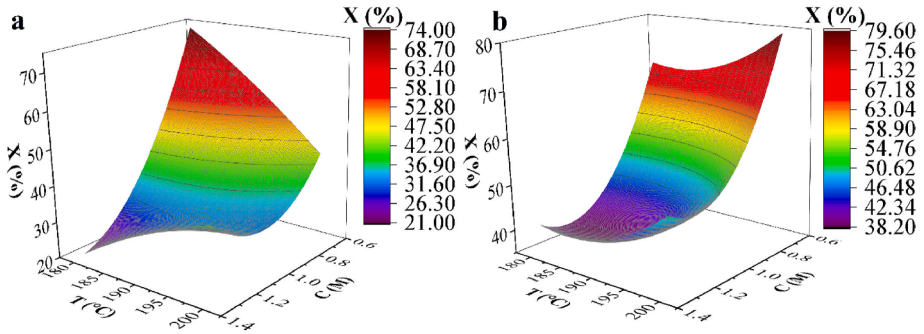

Fig. 3. The simultaneous effect of temperature (X_1, T) and concentration of shaping agent (X_3, C) (a. R1, b. R2, t = 24 h fixed).

efficiency. The highly alkaline medium had a significant contribution to the formation of $Ca(OH)_2$ and TiO_3^{2-} ($Ti(OH)_4 + 2HO^- = TiO_3^{2-} + 3H_2O$) (Wang et al., 2007). The essential role of NaOH in the formation of $CaTiO_3$ seeds was proven by H. Zhao and coworkers by carrying out a blank $CaTiO_3$ synthesis (without NaOH) (Zhao et al., 2013a). Furthermore, it was found that the formation of $CaTiO_3$ can be accelerated using concentrated NaOH (Wang et al., 2007). Additionally, temperature plays a key role in the formation of hydroxide-soluble Na_2TiO_3, because this transformation is endothermic (Prathan et al., 2020).

3.1.1.3. The simultaneous effect of t (X_2) and C (X_3). Analyzing the response surface graphs presented in Fig. 4, we found that the contribution of synthesis duration seems to be almost insignificant in comparison to the concentration of NaOH. Moreover, the detrimental effects of increasing NaOH concentration can be highlighted.

3.1.2. Artificial neural network models

Due to the relatively small data set (26 input–output pairs), the architecture of the trained network was structured as follows: one input, one hidden and one output layer (Fig. 5). While the number of input and output neurons was fixed (i.e., four input neurons: synthesis temperature – X_1, synthesis duration – X_2, concentration of shaping agent – X_3, type of Ca^{2+} source – X_4, 1 output neuron: conversion – X), the number of hidden neurons, activation and training functions were selected by repeated experimentally conducted training tests.

According to the parameters described above, the most efficient FB-ANN architecture was obtained when three hidden neurons, the tangent sigmoid (tansig) transfer function, and the trainoss learning algorithm were used. In this case the determined correlation coefficient for testing was 0.97 (R_{test}), and the mean relative error for testing was 8.80% ($\Delta\varepsilon_{r,mean,\ test}$).

An optimization procedure was also performed by employing the most efficient FB-ANN that we designed. The maximum photocatalytic efficiency (76.2%) was predicted when the following synthesis conditions were applied: 180 °C (X_1), 20 h (X_2), 0.67 M (X_3) and $Ca(NO_3)_2$ (X_4) as the Ca^{2+} source. The optimal synthesis conditions determined in this way overlap with the results from the optimization step based on polynomial regression models. The limitation of the chosen experimental design (i.e., lack of experimental data at the extreme points) was also highlighted in this case.

3.2. Correlations between the morphological, structural, textural, optical properties of the designed $CaTiO_3$ samples and their photocatalytic activity

The main aim of this work was to highlight the correlation between synthesis parameters and photocatalytic efficiency, and between morpho-structural, textural particularities and photocatalytic efficiency by using different modeling approaches. However, this study also provides a brief overview on the cause–effect relationship between the synthesis conditions and morpho-structural particularities of $CaTiO_3$.

The type of Ca^{2+} precursor can have a considerable impact on the morphological, structural, optical and photoelectrochemical properties of the studied material (Wang, S. et al., 2018). To investigate the effect of the Ca^{2+} precursor on morphological and structural properties, SEM micrographs of the samples synthesized according to the central point design (CE, 190 °C, 24 h, 1 M) were com-

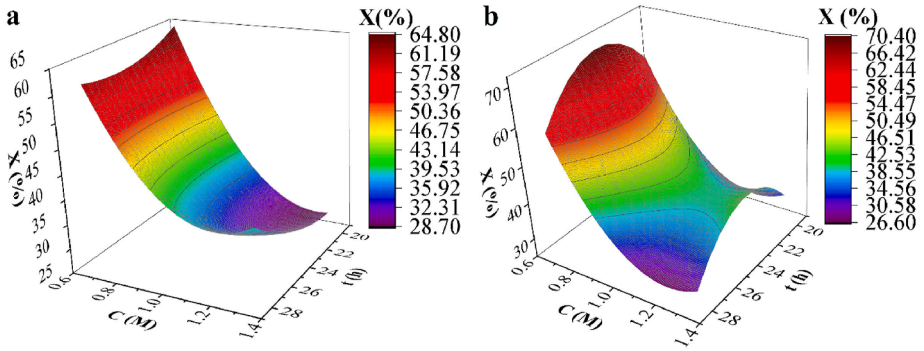

Fig. 4. The simultaneous effect of duration (X_2, t) and concentration of shaping agent (X_3, C) (a. R1, b. R2, T = 190 °C fixed).

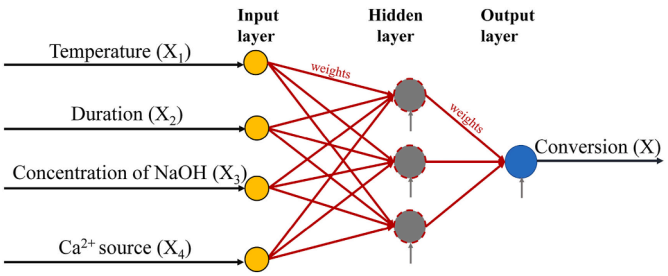

Fig. 5. The architecture of the trained ANN with a maximum number of hidden neurons.

pared. Considering the SEM micrographs, two distinct types of morphology were observed: microrods and square-shaped particles that were not well-defined. Their ratio and arrangement differed for each sample, as they are presented in Fig. 6 a, c – CE1 (R1), Fig. 6 b, d – CE2 (R2). CE1 (Fig. 6 c) had a layered structure, which assured a more ordered aspect for this sample, in comparison to CE2 (Fig. 6 d). The proportion of particles with a not well-defined morphology (square-shaped) was significantly lower in CE1 than that in CE2 (Fig. 6 a, b). Furthermore, while microrods were observed in CE2 (Fig. 6 b), this type of morphology could not be observed in CE1. To have an even more thorough understanding about the morpho-structural properties of the $CaTiO_3$ samples synthesized using different Ca^{2+} sources (CE1, CE2), the crystallite sizes were determined based on the XRD patterns (Fig. 6 e, f) by using the Scherrer equation (Equation (8)). Considering the most intense diffraction peaks within the XRD patterns, the crystallite sizes thus determined were in the range of 20–32 nm in both cases. Although significant differences related to CE1 and CE2 were not expected in terms of optical properties, the absorption spectra in the UV–vis range was considered as an essential part within the characterization of the samples. As anticipated, the studied samples absorbed photons in the UV range, mainly between 250 and 350 nm (Fig. 6 g). The central samples had approximately the same band gap energy values (CE1: 3.6 eV, CE2: 3.5 eV), which were determined based on the reflectance spectra using the Kubelka-Munk function (Equation (9)). These values are in good agreement with the values reported in the scientific literature (Manjunath and G Thimmanna, 2016).

Synthesis temperature can have a considerable effect on the morphology (Dong et al., 2012) and surface features of perovskites (Hernández-Alonso et al., 2011). To investigate this aspect for our $CaTiO_3$ samples (i.e., on their specific surface area, SSA), the SSAs of certain pairs of samples (from R1) were compared. Results were presented in Table 5. In certain cases, considerably higher SSAs were observed for samples synthesized at a higher crystallization temperature (200 °C; case no. 1, 4). However, in other cases, this trend could not be observed (case no. 2, 3). This result was expected because of the interaction effects between the input variables.

The duration of hydrothermal treatment determines the degree of crystallinity (Ebnesajjad and Khaladkar, 2017). According to the literature, enhanced charge transfer (from the center to the surface) and improved photocatalytic activity were observed for highly crystalline samples (Cen et al., 2014). However, before analyzing the crystal phase composition for certain sample pairs (6&15, 7&8), their XRD patterns were evaluated (Fig. 6 e, f). All of reflections identified in the XRD pattern of the studied samples were assigned to the orthorhombic $CaTiO_3$ phase (JCPDS No. 22–0153) (Han et al., 2017). Based on the qualitative analysis of XRD patterns, no significant differences were identified between the samples.

Finally, it is possible to adjust the growth rates of selected crystallographic planes by changing the concentration of a suitable shaping agent (Zhang et al., 2018). According to Table 2, the lowest predefined shaping agent concentration resulted in the desired photocatalytic feature.

3.3. Kinetic modeling

To investigate the photodegradation of RhB, a set of kinetic parameters (pseudo-first order reaction rate constant – k_{obs}, reactant adsorption rate constant – k_{ads}, absolute kinetic constant – k_{degr}, desorption rate constant – k_{des}, light intensity exponent – α) were determined using the mathematical model implemented and validated by Palmisano and coworkers (Palmisano et al., 2015). Understanding the terms linked to the adsorption constant (K_{ads}) has a pivotal role in obtaining an overview on the surface reaction kinetics.

The Langmuir-Hinshelwood approach assumes the balanced adsorption of the reactant molecules ($R_{(liq)} \rightleftharpoons R_{(ads)}$, K_{ads}, described by the ratio between k_{ads} and k_{des}), followed by the rate-controlling step ($R_{(ads)} \rightarrow P$). Recently, the assumption related to the expression of K_{ads} (k_{ads}/k_{des}) has been refuted in the case of most photocatalytic reactions due to the lack of adsorption–desorption equilibria established during photocatalytic reactions (Emeline et al., 2000; Mills et al., 2015; Ollis, 2005, 2018). The pseudo-steady state assumption (PSSA) can be considered as an improved alternative, which considers the dependence of adsorption constant ($K_{ads,\ apparent} = f(I)$, Equation (12)) and Langmuir-Hinshelwood rate constant ($k_{app} = f(I)$) on the light intensity flux (Ollis, 2005, 2018). The validity of PSSA in the case of RhB photodegradation with $CaTiO_3$ perovskites is most likely given by the degradation mechanism (involving free radicals (Deng et al., 2020; Passi and Pal, 2021)).

According to the form of the model (Equation (13)), it is obvious that the observed reaction rate constant, also called as the pseudo-first order reaction rate constant, (k_{obs}) is dependent not only of specific properties of the catalyst (e.g., absorption and scattering coefficient and SSA), but also on the dimensions of the photoreactor (diameter), on the placement of the lamps (distance between them), and on the width of the reactor wall.

The first step within the kinetic modeling was related to the evaluation of kinetic data considering the Langmuir–Hinshelwood mechanism (as depicted in Equations (10) and (11)). The pseudo-first order rate constants (k_{obs}) were determined as the slope of $\ln(C/C_0) = f(t)$ representation). Considering these determined k_{obs} values (presented in the Supplementary Material), it can be reasoned that the higher the conversion of the pollutant, the higher the apparent rate constant is.

The next step was related to the calibration-based optimization. The aim of the optimization problem was to minimize the square difference between the theoretical calculated (*via* Equation (13)) and experimental data-based obtained pseudo-first order reaction rate constant. The computation of k_{obs} assumed the calculation of a double integral, as depicted in Equation (13) considering as integration limits $\theta_0 = 0.358$ rad and l_{1max} (Equation (14)). The numerical integration was performed using 'integral2′ Matlab function. The 'fmincon' Matlab function was used for the calibration-based optimization, considering the predefined upper and lower bounds of the decision variables (k_{ads}: 0–100 $m \cdot h^{-1}$, k_{degr}: 0–0.1 $mmol \cdot m^{-2(1-\alpha)} \cdot W^{-\alpha} \cdot h^{-1}$, k_{des}:0–500 $mmol \cdot m^{-2} \cdot h^{-1}$, α: 0.5–1). The initial values for the kinetic parameters were taken from the literature: $k_{ads} = 19.6\ m \cdot h^{-1}$, $k_{des} = 92.2\ mmol \cdot m^{-2} \cdot h^{-1}$, $k_{degr} = 1.62 \cdot 10^{-2}\ mmol \cdot m^{-2(1-\alpha)} \cdot W^{-\alpha} \cdot h^{-1}$, $\alpha = 0.5$. Considering the higher determination coefficients for the computation of k_{obs} in the case of R1 (Supplementary Material), the kinetic parameters (k_{ads}, k_{degr}, k_{des}, α) were determined for this case.

During the calibration-based optimization, the following assumptions have been considered.

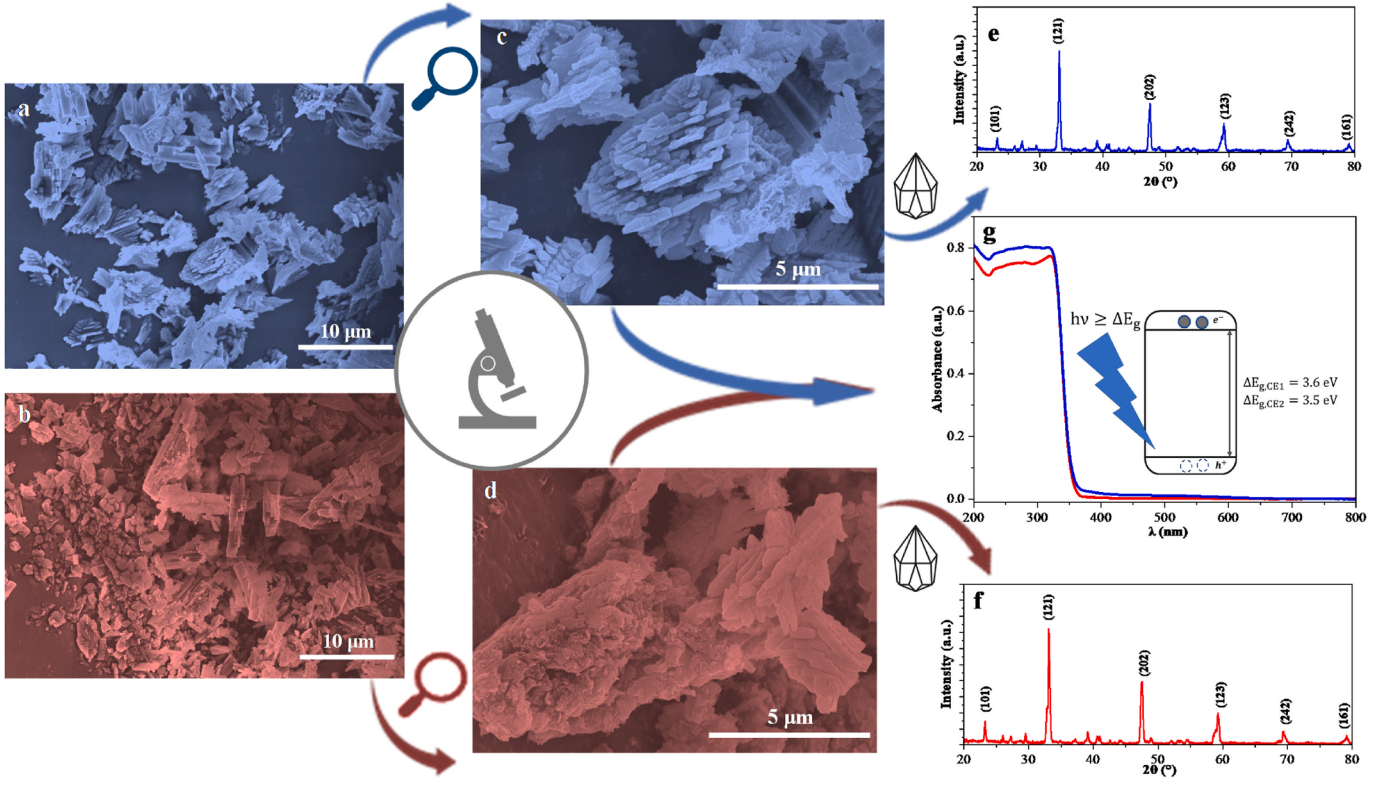

Fig. 6. a-d. SEM micrographs (CE1: a, c; CE2: b, d), e-f. XRD patterns (CE1: e, CE2: f), g. UV–Vis spectra (CE1 and CE2).

Table 5
Specific surface areas of certain pairs of samples from R1.

Case no.	t (h)	C (M)	T = 180 °C	T = 200 °C
			SSA ($m^2 \cdot g^{-1}$)	
1	24	0.670	9.9 (E2)	18.9 (E1)
2	24	1.340	22.2 (E13)	10.2 (E3)
3	28	1.005	11.3 (E5)	10.1 (E4)
4	20	1.005	56.6 (E12)	111.5 (E14)

i) Perfect mixing.
ii) Constant temperature of the reaction mixture.
iii) Constant absorption coefficient for the cases of all samples (due to the similar shape and size of the catalysts (Bloh, 2021; Cabrera et al., 1996))
iv) Langmuir-Hinshelwood mechanism, PSSA.
v) Monochromatic irradiation (λ_{max} = 365 nm).

First, the correlation between photocatalytic activity and SSA was investigated in the case of the studied samples and this is presented in Fig. 7. Enhanced photocatalytic activity and large SSA were linked in many scientific works, which was explained mainly by the excessive number of active sites (Cheng et al., 2014; Tian et al., 2008). However, the validity of correlation would require very similar crystallinity, facet distribution and defects (Bloh, 2021; Wilmer et al., 2003). As can be observed in Fig. 7, there was no correlation between SSA and photocatalytic efficiency in the case of $CaTiO_3$ samples synthesized according to DoE (R1).

The k_{ads}, k_{des} values (determined from calibration-based optimization) were correlated with SSA. This is presented in Fig. 8. While the k_{ads} values were situated between 0.10 and 0.67 $m \cdot h^{-1}$, the k_{des} had the values varying in the range of 79–150 $mmol \cdot m^{-2} \cdot h^{-1}$. According to Fig. 8, it can be observed that a higher SSA led to lower k_{ads} and higher k_{des}. The reason for this correlation relies on the relationship between SSA, surface tension and rate of adsorption/desorption processes. While low SSA is associated with high surface tension (and implicitly high adsorption rate – high k_{ads}), high SSA is linked to low surface tension (high desorption rate – high k_{des}) (Ward and Tordai, 1946). Furthermore, the formation of intermediates during degradation (and adsorbed on the surface of the catalyst) can influence on the rate of surface processes (adsorption-desorption).

Although the adsorption and desorption processes (expressed *via* k_{ads} and k_{des}) have considerable significance in photocatalytic processes, the decisive parameter is k_{degr}. Fig. 9 provides a clear overview on the correlation between X and k_{degr}. As expected, a higher X resulted in a higher k_{degr}. Furthermore, the fitted value of α was in the range situated between 0.54 and 0.55, which provided a direct indication about the high intensity conditions (Mills and Le Hunte, 1997).

4. Conclusions

The present work highlighted that the appropriate selection of synthesis conditions could improve the photocatalytic activity of the hydrothermally obtained $CaTiO_3$. Second-order polynomial regression and artificial neural network models were applied to establish correlations between selected synthesis parameters (T, t, C_{NaOH}, Ca^{2+} precursor type) and photocatalytic activity of $CaTiO_3$ for rhodamine B degradation, which were further used for optimization. Thirty hydrothermal syntheses were performed according to the Box-Behnken design, followed by the assessment of photocatalytic performance (20–80% conversion). Considering the most favor-

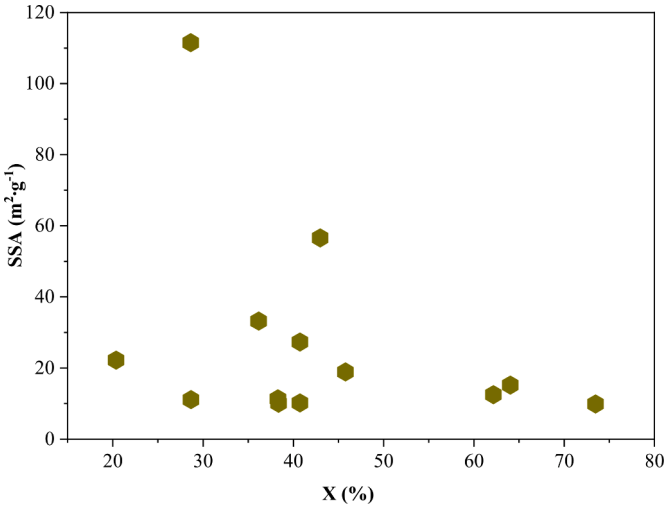

Fig. 7. Correlation between conversion (X) and specific surface area (SSA) in the case of R1.

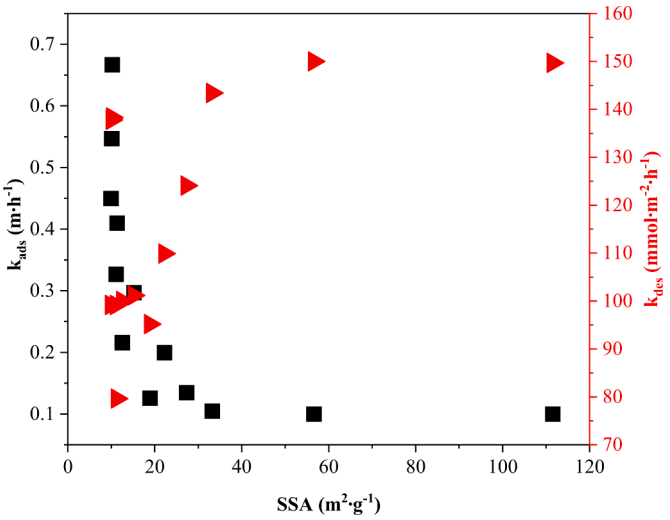

Fig. 8. Correlation between specific surface area (SSA) and the computed adsorption, desorption kinetic constants (k_{ads}, k_{des}) in the case of R1.

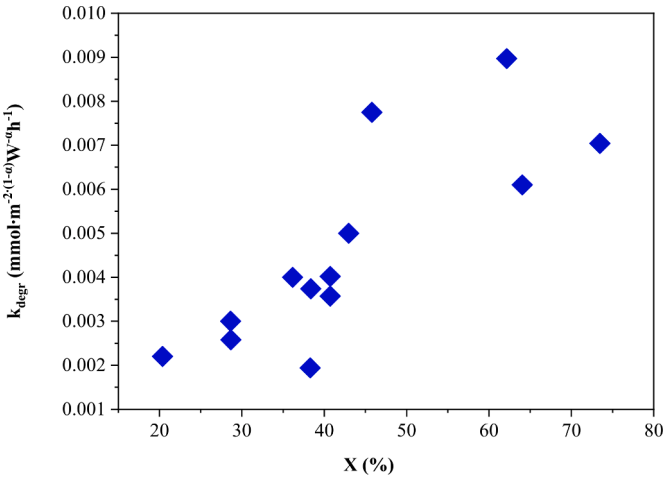

Fig. 9. Correlation between conversion (X) and the computed absolute kinetic constant (k_{degr}) in the case of R1.

able synthesis conditions determined from optimization (200 °C, 23.7 h, 0.67 M, $CaCl_2$ precursor), the photocatalytic efficiency of the subsequently synthesized and experimentally validated $CaTiO_3$ catalyst was ~96%. To overview the morphological, structural, and optical peculiarities, selected $CaTiO_3$ samples were analyzed by complementary methods (i.e., SEM: square-shaped particles, XRD: orthorhombic crystal phase, N_2 sorption – SSA: 10–120 $m^2 \cdot g^{-1}$, DRS – ΔE_g: 3.5–3.6 eV). Finally, specific kinetic parameters (i.e., adsorption – k_{ads}: 0.10–0.67 $m \cdot h^{-1}$ and desorption – k_{des}: 79–150 $mmol \cdot m^{-2} \cdot h^{-1}$, absolute kinetic rate constant – k_{degr}: 0.001–0.010 $mmol \cdot m^{-2(1-\alpha)} \cdot W^{-\alpha} \cdot h^{-1}$) were determined using a validated mathematical model from the literature considering the Langmuir-Hinshelwood mechanism and the pseudo-steady state assumptions. The following conclusions were deduced based on the kinetic modeling: (1) the higher the photocatalytic activity, the higher the absolute kinetic rate constant was; (2) with increasing specific surface area the rate of adsorption decreased and that of desorption increased.

Authors' contribution

Bíborka Boga – Writing: original draft, review and analysis, Investigation, Formal analysis, Methodology. **Vasile-Mircea Cristea:** Conceptualization, Supervision, Writing – review and analysis. **István Székely** – Methodology, Formal analysis, Writing: review and analysis. **Felix Lorenz** – Investigation (BET), Writing: review and analysis. **Tamás Gyulavári** – Investigation (SEM), Writing: review and analysis, **Lucian Cristian Pop** – Writing: review and analysis, **Lucian Baia** – Supervision. Writing: review and analysis, Funding acquisition. **Zsolt Pap** – Conceptualization, Methodology, Writing: review and analysis, Funding acquisition. **Norbert Steinfeldt** – Writing: review and analysis, Supervision, Funding acquisition. **Jennifer Strunk**: Writing: review and analysis, Funding acquisition.

Funding

This research did not receive any specific grant from funding agencies in the public, commercial, or not-for-profit sectors.

Declaration of competing interest

The authors declare that they have no known competing financial interests or personal relationships that could have appeared to influence the work reported in this paper.

Data availability

No data was used for the research described in the article.

Acknowledgements

Bíborka Boga expresses her gratitude towards her colleagues, M.Sc. Eng. Kata Saszet (PhD Student) and Dr. Klára Magyari for their help during the recording of XRD patterns. Furthermore, Bíborka Boga is grateful for the help in formatting the manuscript provided by her colleague, M.Sc. Shuoping Ding (PhD Student).

Bíborka Boga gratefully acknowledges the financial support provided by Márton Áron Szakkollégium, funded by the Hungarian Ministry of Foreign Affairs and Trade, during the 2021–2022 and 2022–2023 academic years. Furthermore, Bíborka Boga expresses her gratitude towards the German Federal Environmental Foundation (Deutsche Bundesstiftung Umwelt) for the provided fellowship during the 2021–2022 academic year. Tamás Gyulavári is grateful for the financial support of the NKFI-PD-138248 project. The authors acknowledge the 2019-2.1.13-TÉT_IN-2020-00015 project.

Appendix A. Supplementary data

Supplementary data to this article can be found online at https://doi.org/10.1016/j.scp.2023.101045.

References

Bai, L., Xu, Q., Cai, Z., 2018. Synthesis of Ag@ AgBr/$CaTiO_3$ composite photocatalyst with enhanced visible light photocatalytic activity. J. Mater. Sci. Mater. Electron. 29 (20), 17580–17590. https://doi.org/10.1007/s10854-018-9861-y.

Biegalski, M.D., Qiao, L., Gu, Y., Mehta, A., He, Q., Takamura, Y., Borisevich, A., Chen, L.-Q., 2015. Impact of symmetry on the ferroelectric properties of $CaTiO_3$ thin films. Appl. Phys. Lett. 106 (16), 162904. https://doi.org/10.1063/1.4918805.

Bloh, J.Z., 2021. Intensification of heterogeneous photocatalytic reactions without efficiency losses: the importance of surface catalysis. Catal. Lett. 151, 3105–3113. https://doi.org/10.1007/s10562-021-03573-0.

Cabrera, M.I., Alfano, O.M., Cassano, A.E., 1996. Absorption and scattering coefficients of titanium dioxide particulate suspensions in water. J. Phys. Chem. 100 (51), 20043–20050. https://doi.org/10.1021/jp962095q.

Cen, W., Xiong, T., Tang, C., Yuan, S., Dong, F., 2014. Effects of morphology and crystallinity on the photocatalytic activity of $(BiO)_2CO_3$ nano/microstructures. Ind. Eng. Chem. Res. 53 (39), 15002–15011. https://doi.org/10.1021/ie502670n.

Chen, T., Meng, J., Wu, S., Pei, J., Lin, Q., Wei, X., Li, J., Zhang, Z., 2018. Room temperature synthesized $BaTiO_3$ for photocatalytic hydrogen evolution. J. Alloys Compd. 754, 184–189. https://doi.org/10.1016/j.jallcom.2018.04.300.

Cheng, H., Wang, J., Zhao, Y., Han, X., 2014. Effect of phase composition, morphology, and specific surface area on the photocatalytic activity of TiO_2 nanomaterials. RSC Adv. 4 (87), 47031–47038. https://doi.org/10.1039/C4RA05509H.

Cui, L., Hui, K., Hui, K., Lee, S., Zhou, W., Wan, Z., Thuc, C.-N.H., 2012. Facile microwave-assisted hydrothermal synthesis of TiO_2 nanotubes. Mater. Lett. 75, 175–178. https://doi.org/10.1016/j.matlet.2012.02.004.

da Silva, L.F., Lopes, O.F., de Mendonça, V.R., Carvalho, K.T., Longo, E., Ribeiro, C., Mastelaro, V.R., 2016. An understanding of the photocatalytic properties and pollutant degradation mechanism of $SrTiO_3$ nanoparticles. Photochem. Photobiol. 92 (3), 371–378. https://doi.org/10.1111/php.12586.

de Cássia Pereira, S., De Figueiredo, A.T., Barrado, C.M., Stoppa, M.H., Dos Santos, T.O., Pontes, F.M., Longo, E., 2017. Fast and efficient microwave-assisted synthesis of $CaTiO_3$. Mater. Res. Express 4 (6), 065014. https://doi.org/10.1088/2053-1591/aa7483.

Deng, B., Si, P., Bauman, L., Luo, J., Rao, M., Peng, Z., Jiang, T., Li, G., Zhao, B., 2020. Photocatalytic activity of $CaTiO_3$ derived from roasting process of bauxite residue. J. Clean. Prod. 244, 118598. https://doi.org/10.1016/j.jclepro.2019.118598.

Deshpande, P.A., Madras, G., 2010. Photocatalytic degradation of dyes over combustion-synthesized $Ce_{1-x}Fe_xVO_4$. Chem. Eng. J. 158 (3), 571–577. https://doi.org/10.1016/j.cej.2010.01.056.

Dillon, W.R., Goldstein, M., 1984. Multivariate Analysis: Methods and Applications. Wiley, New York, ISBN 978-0-471-08317-7.

Dobre, T.G., Marcano, J.G.S., 2007. Chemical Engineering: Modeling, Simulation and Similitude. John Wiley & Sons, Weinheim, ISBN 978-3-527-30607-7.

Dong, W., Song, B., Meng, W., Zhao, G., Han, G., 2015. A simple solvothermal process to synthesize $CaTiO_3$ microspheres and its photocatalytic properties. Appl. Surf. Sci. 349, 272–278. https://doi.org/10.1016/j.apsusc.2015.05.006.

Dong, W., Zhao, G., Song, B., Xu, G., Zhou, J., Han, G., 2012. Surfactant-free fabrication of $CaTiO_3$ butterfly-like dendrite via a simple one-step hydrothermal route. CrystEngComm 14 (20), 6990–6997. https://doi.org/10.1039/C2CE25472G.

Ebnesajjad, S., Khaladkar, P.R., 2017. Fluoropolymer Applications in the Chemical Processing Industries: the Definitive User's Guide and Handbook. William Andrew, Oxford, ISBN 978-0-323-447-16-4.

Edwards, D., Hamson, M., 2020. Guide to Mathematical Modelling. Bloomsbury, London, ISBN 978-0-333-79446-3.

Emeline, A.V., Ryabchuk, V., Serpone, N., 2000. Factors affecting the efficiency of a photocatalyzed process in aqueous metal-oxide dispersions: prospect of distinguishing between two kinetic models. J. Photochem. Photobiol. Chem. 133 (1–2), 89–97. https://doi.org/10.1016/S1010-6030(00)00225-2.

Fogler, H.S., 2010. Essentials of Chemical Reaction Engineering: Essenti Chemica Reactio Engi. Pearson Education, New York, ISBN 978-0-13-714612-3.

Han, C., Liu, J., Yang, W., Wu, Q., Yang, H., Xue, X., 2016. Enhancement of photocatalytic activity of $CaTiO_3$ through HNO_3 acidification. J. Photochem. Photobiol. Chem. 322, 1–9. https://doi.org/10.1016/j.jphotochem.2016.02.012.

Han, C., Liu, J., Yang, W., Wu, Q., Yang, H., Xue, X., 2017. Photocatalytic activity of $CaTiO_3$ synthesized by solid state, sol–gel and hydrothermal methods. J. Sol. Gel Sci. Technol. 81 (3), 806–813. https://doi.org/10.1007/s10971-016-4261-3.

Hernández-Alonso, M., García-Rodríguez, S., Sánchez, B., Coronado, J., 2011. Revisiting the hydrothermal synthesis of titanate nanotubes: new insights on the key factors affecting the morphology. Nanoscale 3 (5), 2233–2240. https://doi.org/10.1039/C1NR10081E.

Hossain, F., 2018. Sustainable Design and Build: Building, Energy, Roads, Bridges, Water and Sewer Systems. Butterworth-Heinemann, New York, ISBN 978-0-12-816722-9.

Huang, X.-J., Xin, Y., Wu, H.-Y., Ying, F., Min, Y.-H., Li, W.-S., Wang, S.-Y., Wu, Z.-J., 2016. Preparation of Zr-doped $CaTiO_3$ with enhanced charge separation efficiency

and photocatalytic activity. Trans. Nonferrous Metals Soc. China 26 (2), 464–471. https://doi.org/10.1016/S1003-6326(16)64097-9.
Huo, Y., Yang, H., Xian, T., Jiang, J., Wei, Z., Li, R., Feng, W., 2014. A polyacrylamide gel route to different-sized $CaTiO_3$ nanoparticles and their photocatalytic activity for dye degradation. J. Sol. Gel Sci. Technol. 71 (2), 254–259. https://doi.org/10.1007/s10971-014-3366-9.
Jang, J., Borse, P., Lee, J.S., Lim, K., Jung, O., Jeong, E., Bae, J., Kim, H., 2011. Photocatalytic hydrogen production in water-methanol mixture over iron-doped $CaTiO_3$. Bull. Kor. Chem. Soc. 32 (1), 95–99. . eISSN: 1229-5949.
Joo, J.B., Zhang, Q., Dahl, M., Lee, I., Goebl, J., Zaera, F., Yin, Y., 2012. Control of the nanoscale crystallinity in mesoporous TiO_2 shells for enhanced photocatalytic activity. Energy Environ. Sci. 5 (4), 6321–6327. https://doi.org/10.1039/C1EE02533C.
Kappadan, S., Gebreab, T.W., Thomas, S., Kalarikkal, N., 2016. Tetragonal $BaTiO_3$ nanoparticles: an efficient photocatalyst for the degradation of organic pollutants. Mater. Sci. Semicond. Process. 51, 42–47. https://doi.org/10.1016/j.mssp.2016.04.019.
Kedves, E.-Z., Székely, I., Baia, L., Baia, M., Csavdári, A., Pap, Z., 2019. The comparison of the photocatalytic performance shown by TiO_2 and TiO_2/WO_3 composites—a parametric and kinetic study. J. Nanosci. Nanotechnol. 19 (1), 356–365. https://doi.org/10.1166/jnn.2019.15792.
Kimijima, T., Kanie, K., Nakaya, M., Muramatsu, A., 2014. Hydrothermal synthesis of size-and shape-controlled $CaTiO_3$ fine particles and their photocatalytic activity. CrystEngComm 16 (25), 5591–5597. https://doi.org/10.1039/C4CE00376D.
Koutsoukos, P.G., Kofina, A.N., Kanellopoulou, D.G., 2007. Solubility of salts in water: key issue for crystal growth and dissolution processes. Pure Appl. Chem. 79 (5), 825–850. https://doi.org/10.1351/pac200779050825.
Kumar, A., Kumar, A., Krishnan, V., 2020. Perovskite oxide based materials for energy and environment-oriented photocatalysis. ACS Catal. 10 (17), 10253–10315. https://doi.org/10.1021/acscatal.0c02947.
Lee, S., Kwak, S., Park, T., Son, B., Yun, H.J., Hur, J., Yoo, H., 2021. Synthesis of lead-free $CaTiO_3$ oxide perovskite film through solution combustion method and its thickness-dependent hysteresis behaviors within 100 mV operation. Molecules 26 (18), 5446. https://doi.org/10.3390/molecules26185446.
Luo, C., Zhao, J., Li, Y., Zhao, W., Zeng, Y., Wang, C., 2018. Photocatalytic CO_2 reduction over $SrTiO_3$: correlation between surface structure and activity. Appl. Surf. Sci. 447, 627–635. https://doi.org/10.1016/j.apsusc.2018.04.049.
Maddu, A., Permatasari, L., Arif, A., 2017. Structural and dielectric properties of $CaTiO_3$ synthesized utilizing Duck's eggshell as a calcium source. J. Ceram. Process. Res. 18 (2), 146–150.
Manjunath, K., G Thimmanna, C., 2016. Studies on synthesis, characterization and applications of nano $CaTiO_3$ powder. Curr. Nanomater. 1 (2), 145–155. https://doi.org/10.2174/2405461501666160805125748.
Mehrizad, A., Gharbani, P., 2014. Decontamination of 4-chloro-2-nitrophenol from aqueous solution by graphene adsorption: equilibrium, kinetic, and thermodynamic studies. Pol. J. Environ. Stud. 23 (6). https://doi.org/10.15244/pjoes/26779.
Mehrizad, A., Gharbani, P., 2016. Application of central composite design and artificial neural network in modeling of reactive blue 21 dye removal by photo-ozonation process. Water Sci. Technol. 74 (1), 184–193. https://doi.org/10.2166/wst.2016.199.
Mehrizad, A., Gharbani, P., 2017. Novel ZnS/carbon nanofiber photocatalyst for degradation of rhodamine 6G: kinetics tracking of operational parameters and development of a kinetics model. Photochem. Photobiol. 93 (5), 1178–1186. https://doi.org/10.1111/php.12795.
Mills, A., Le Hunte, S., 1997. An overview of semiconductor photocatalysis. J. Photochem. Photobiol. Chem. 108 (1), 1–35. https://doi.org/10.1016/S1010-6030(97)00118-4.
Mills, A., O'Rourke, C., Moore, K., 2015. Powder semiconductor photocatalysis in aqueous solution: an overview of kinetics-based reaction mechanisms. J. Photochem. Photobiol. Chem. 310, 66–105. https://doi.org/10.1016/j.jphotochem.2015.04.011.
Monshi, A., Foroughi, M.R., Monshi, M.R., 2012. Modified Scherrer equation to estimate more accurately nano-crystallite size using XRD. World J. Nano Sci. Eng. 2 (3), 154–160. https://doi.org/10.4236/wjnse.2012.23020.
Mosavi, S.A., Ghadi, A., Gharbani, P., Mehrizad, A., 2021. Photocatalytic removal of Methylene Blue using Ag@ CdSe/Zeoilte nanocomposite under visible light irradiation by Response Surface Methodology. Mater. Chem. Phys. 267, 124696. https://doi.org/10.1016/j.matchemphys.2021.124696.
Naik, A.P., Mittal, H., Wadi, V.S., Sane, L., Raj, A., Alhassan, S.M., Al Alili, A., Bhosale, S.V., Morajkar, P.P., 2020. Super porous TiO_2 photocatalyst: tailoring the agglomerate porosity into robust structural mesoporosity with enhanced surface area for efficient remediation of azo dye polluted waste water. J. Environ. Manag. 258, 110029. https://doi.org/10.1016/j.jenvman.2019.110029.
Ollis, D.F., 2005. Kinetics of liquid phase photocatalyzed reactions: an illuminating approach. J. Phys. Chem. B 109 (6), 2439–2444. https://doi.org/10.1021/jp040236f.
Ollis, D.F., 2018. Kinetics of photocatalyzed reactions: five lessons learned. Front. Chem. 6, 378. https://doi.org/10.3389/fchem.2018.00378.
Palmisano, G., Loddo, V., Augugliaro, V., Bellardita, M., Roda, G.C., Parrino, F., 2015. Validation of a two-dimensional modeling of an externally irradiated slurry photoreactor. Chem. Eng. J. 262, 490–498. https://doi.org/10.1016/j.cej.2014.10.013.
Passi, M., Pal, B., 2021. A review on $CaTiO_3$ photocatalyst: activity enhancement methods and photocatalytic applications. Powder Technol. 388, 274–304. https://doi.org/10.1016/j.powtec.2021.04.056.
Peng, X., Yang, G., Shi, Y., Zhou, Y., Zhang, M., Li, S., 2020. Box–Behnken design based statistical modeling for the extraction and physicochemical properties of pectin from sunflower heads and the comparison with commercial low-methoxyl pectin. Sci. Rep. 10 (1), 1–10. https://doi.org/10.1038/s41598-020-60339-1.
Perez-Rodriguez, F., Valero, A., 2013. Predictive Microbiology in Foods. Springer, New York, ISBN 978-1-4614-5519-6.
Prathan, A., Sanglao, J., Wang, T., Bhoomanee, C., Ruankham, P., Gardchareon, A., Wongratanaphisan, D., 2020. Controlled structure and growth mechanism behind hydrothermal growth of TiO_2 nanorods. Sci. Rep. 10 (1), 1–11. https://doi.org/10.1038/s41598-020-64510-6.
Sematech, N., 2006. Engineering statistics handbook. NIST SEMATECH. https://doi.org/10.18434/M32189.
Shimura, K., Yoshida, H., 2010. Hydrogen production from water and methane over Pt-loaded calcium titanate photocatalyst. Energy Environ. Sci. 3 (5), 615–617. https://doi.org/10.1039/B922793H.
Solís, R.R., Bedia, J., Rodríguez, J.J., Belver, C., 2021. A review on alkaline earth metal titanates for applications in photocatalytic water purification. Chem. Eng. J. 409, 128110. https://doi.org/10.1016/j.cej.2020.128110.
Soltani, T., Zhu, X., Yamamoto, A., Singh, S.P., Fudo, E., Tanaka, A., Kominami, H., Yoshida, H., 2021. Effect of transition metal oxide cocatalyst on the photocatalytic activity of Ag loaded $CaTiO_3$ for CO_2 reduction with water and water splitting. Appl. Catal. B Environ. 286, 119899. https://doi.org/10.1016/j.apcatb.2021.119899.
Tabatabaei, S., Dastmalchi, S., Mehrizad, A., Gharbani, P., 2011. Enhancement of 4-nitrophenol ozonation in water by nano ZnO catalyst. Iran. J. Environ. Health Sci. Eng. 8 (4), 363–372.
Tian, G., Fu, H., Jing, L., Xin, B., Pan, K., 2008. Preparation and characterization of stable biphase TiO_2 photocatalyst with high crystallinity, large surface area, and enhanced photoactivity. J. Phys. Chem. C 112 (8), 3083–3089. https://doi.org/10.1021/jp710283p.
Wang, D., Guo, Z., Chen, Y., Hao, J., Liu, W., 2007. In situ hydrothermal synthesis of nanolamellate $CaTiO_3$ with controllable structures and wettability. Inorg. Chem. 46 (19), 7707–7709. https://doi.org/10.1021/ic700777f.
Wang, R., Ni, S., Liu, G., Xu, X., 2018a. Hollow $CaTiO_3$ cubes modified by La/Cr co-doping for efficient photocatalytic hydrogen production. Appl. Catal. B Environ. 225, 139–147. https://doi.org/10.1016/j.apcatb.2017.11.061.
Wang, S., Kuang, P., Cheng, B., Yu, J., Jiang, C., 2018b. ZnO hierarchical microsphere for enhanced photocatalytic activity. J. Alloys Compd. 741, 622–632. https://doi.org/10.1016/j.jallcom.2018.01.141.
Ward, A., Tordai, L., 1946. Time-dependence of boundary tensions of solutions I. The role of diffusion in time-effects. J. Chem. Phys. 14 (7), 453–461. https://doi.org/10.1063/1.1724167.
Wilmer, H., Kurtz, M., Klementiev, K., Tkachenko, O., Grünert, W., Hinrichsen, O., Birkner, A., Rabe, S., Merz, K., Driess, M., 2003. Methanol synthesis over ZnO: a structure-sensitive reaction? Phys. Chem. Chem. Phys. 5 (20), 4736–4742. https://doi.org/10.1039/B304425D.
Xing, G., Zhao, L., Sun, T., Su, Y., Wang, X., 2016. Hydrothermal derived nitrogen doped $SrTiO_3$ for efficient visible light driven photocatalytic reduction of chromium (VI). SpringerPlus 5 (1), 1–13. https://doi.org/10.1186/s40064-016-2804-2.
Yang, H., Han, C., Xue, X., 2014. Photocatalytic activity of Fe-doped $CaTiO_3$ under UV–visible light. J. Environ. Sci. 26 (7), 1489–1495. https://doi.org/10.1016/j.jes.2014.05.015.

Yang, X., Fu, J., Jin, C., Chen, J., Liang, C., Wu, M., Zhou, W., 2010. Formation mechanism of $CaTiO_3$ hollow crystals with different microstructures. J. Am. Chem. Soc. 132 (40), 14279–14287. https://doi.org/10.1021/ja106461u.

Yin, P., Fan, X., 2001. Estimating R^2 shrinkage in multiple regression: a comparison of different analytical methods. J. Exp. Educ. 69 (2), 203–224. https://doi.org/10.1080/00220970109600656.

Yu, K., Zhang, C., Chang, Y., Feng, Y., Yang, Z., Yang, T., Lou, L.-L., Liu, S., 2017. Novel three-dimensionally ordered macroporous $SrTiO_3$ photocatalysts with remarkably enhanced hydrogen production performance. Appl. Catal. B Environ. 200, 514–520. https://doi.org/10.1016/j.apcatb.2016.07.049.

Zhang, J., Huang, K., Yuan, L., Feng, S., 2018. Mineralizer effect on facet-controllable hydrothermal crystallization of perovskite structure $YbFeO_3$ crystals. CrystEngComm 20 (4), 470–476. https://doi.org/10.1039/C7CE01827D.

Zhang, Q., Li, Y., Ren, Z., Ahmad, Z., Li, X., Han, G., 2015. Synthesis of porous $CaTiO_3$ nanotubes with tunable hollow structures via single-nozzle electrospinning. Mater. Lett. 152, 82–85. https://doi.org/10.1016/j.matlet.2015.03.103.

Zhao, H., Duan, Y., Sun, X., 2013. Synthesis and characterization of $CaTiO_3$ particles with controlled shape and size. New J. Chem. 37 (4), 986–991. https://doi.org/10.1039/C3NJ40974K.

Zhu, Y., Wang, X., Zhou, Y., Zhao, C., Yuan, J., Wu, Z., Wu, S., Wang, S., 2016. In situ formation of bioactive calcium titanate coatings on titanium screws for medical implants. RSC Adv. 6 (58), 53182–53187. https://doi.org/10.1039/C6RA06597J.